Shallow Dynamic Overshoot and Energetic Deep Rupture in the 2011 M_w 9.0 Tohoku-Oki Earthquake

Satoshi Ide,[1]* Annemarie Baltay,[2] Gregory C. Beroza[2]

Strong spatial variation of rupture characteristics in the moment magnitude (M_w) 9.0 Tohoku-Oki megathrust earthquake controlled both the strength of shaking and the size of the tsunami that followed. Finite-source imaging reveals that the rupture consisted of a small initial phase, deep rupture for up to 40 seconds, extensive shallow rupture at 60 to 70 seconds, and continuing deep rupture lasting more than 100 seconds. A combination of a shallow dipping fault and a compliant hanging wall may have enabled large shallow slip near the trench. Normal faulting aftershocks in the area of high slip suggest dynamic overshoot on the fault. Despite prodigious total slip, shallower parts of the rupture weakly radiated at high frequencies, whereas deeper parts of the rupture radiated strongly at high frequencies.

The 11 March 2011 moment magnitude (M_w) 9.0 Tohoku-Oki Earthquake occurred on the Japan Trench plate boundary off the eastern shore of northern Honshu. The mainshock was preceded by a foreshock sequence lasting 2 days. The largest of these was an M_w 7.3 earthquake on 9 March 2011. This foreshock and the mainshock share similar low-angle thrust mechanisms, and their epicenters are separated by only ~45 km (Fig. 1). Earthquake-scaling relations suggest a characteristic fault plane dimension of ~50 km for an M_w 7.3 earthquake (*1*, *2*), and the initial rupture point of the mainshock is close to the rupture area of the foreshock. The relative size, proximity, and similarity of the two events allows us to use the foreshock as an empirical Green's function (eGf) (*3*–*7*) to study the source process of the mainshock.

The eGf approach assumes that waveforms from a small earthquake (eGf event) approximate the point dislocation response from points near the source of the eGf event, once the appropriate time shift due to the location difference is taken into account. An advantage of this method over numerical seismogram simulation is that we do not have to model the effects of complex Earth structure. The Tohoku-Oki earthquake started with relatively small amplitude arrivals during the first 3 s that are only clearly visible at seismically quiet stations (fig. S1). Thereafter, the earthquake quickly grew into a large event.

We inverted broadband seismograms at 50 Global Seismographic Network (GSN) stations (fig. S2) to image the spatio-temporal slip distribution shown in Fig. 1 (*8*). After the weak initial phase, the mainshock rupture propagated downdip toward the island of Honshu and reached a

[1]Department of Earth and Planetary Science, University of Tokyo, Hongo 7-3-1, Bunkyo-ku, Tokyo 113-0033, Japan. [2]Department of Geophysics, Stanford University, 397 Panama Mall, Stanford, CA 94305–2215, USA.

*To whom correspondence should be addressed. E-mail: ide@eps.s.u-tokyo.ac.jp

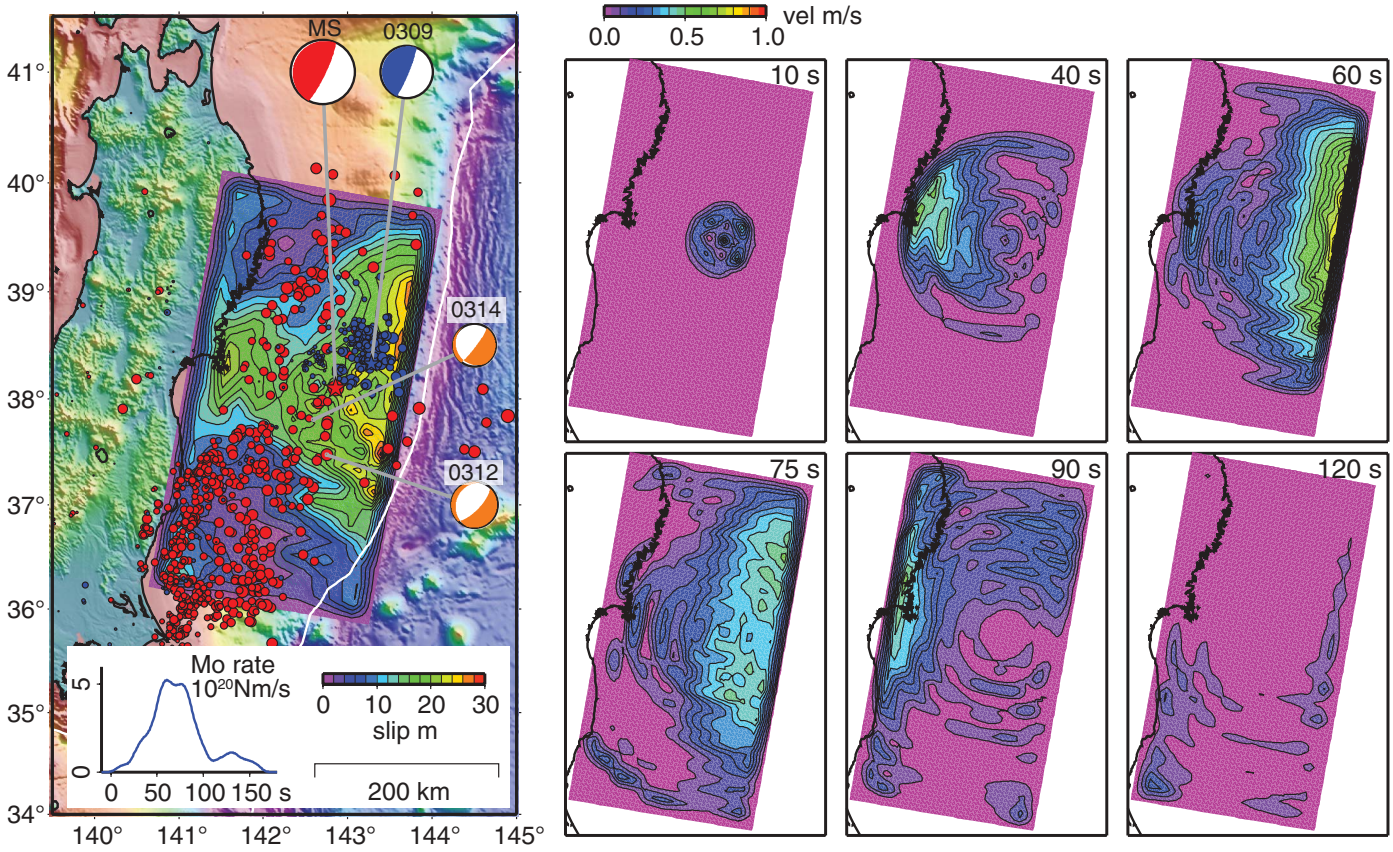

Fig. 1. The total slip distribution (**left**) and snapshots of the slip-rate distribution at six different times (**right**). Blue/white (0309), red/white (MS), and orange/white circles (0312 and 0314) show focal mechanisms of the foreshock on 9 March (M_w 7.3), the mainshock, and two aftershocks with opposite mechanism on 12 March (M_w 6.5) and 14 March (M_w 6.1), connected to their epicenters with gray lines. Circles are epicenters determined by the Japan Meteorological Agency. Smaller red circles are the mainshock (star) and aftershocks; smaller blue circles are the largest foreshock (star) and foreshocks. The fault plane is 440 by 220 km. A blue curve in the inset shows the global-moment rate function, which is the moment rate observed in the far-field perpendicular to the fault.

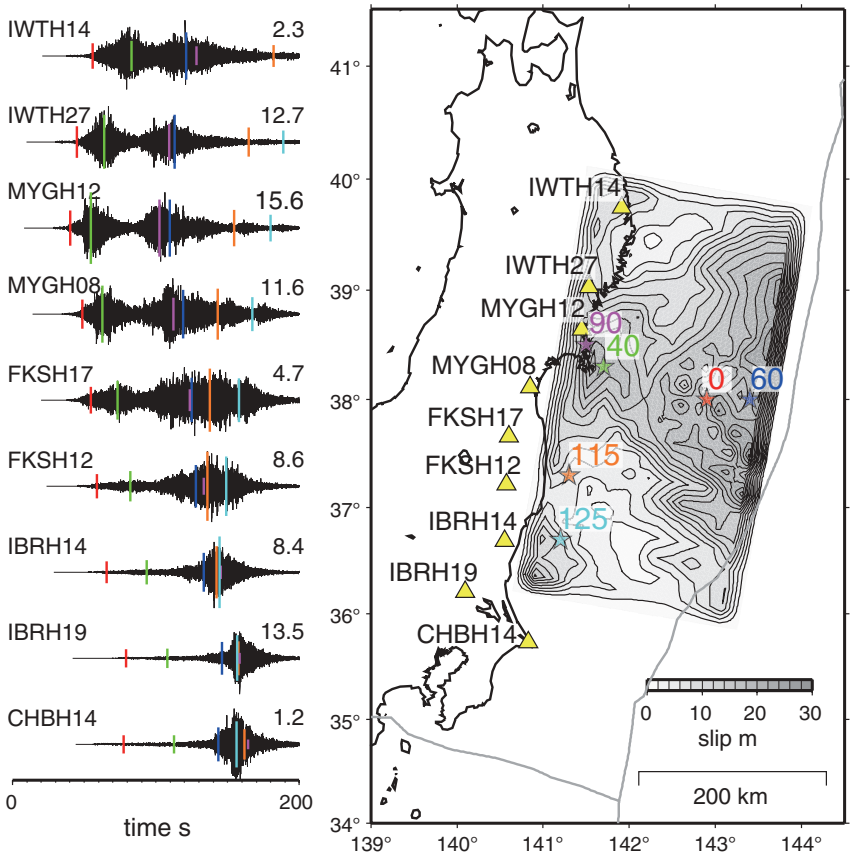

Fig. 2. (**Left**) Strong motion records high-pass filtered above 10 Hz at nine KiK-net stations of the National Research Institute for Earth Science and Disaster Prevention distributed along the rupture. The maximum amplitude in centimeters per second per second is shown at the top-right of each waveform. (**Right**) Mainshock slip distribution. The *S*-wave arrival times from several source locations, denoted with colored stars and with time after the rupture initiation also shown, are plotted on the waveforms with length inversely proportional to the source-station distance.

local maximum in slip rate at ~40 s before propagating back up-dip toward the shallower region to the trench axis where the slip rate reached a maximum of ~0.9 m/s at 60 s. The shallow large slip appears to emerge suddenly because up-dip rupture propagation before 40 s is not well resolved, perhaps due to smaller slip rate than that of the deep rupture. We suggest that the rupture front propagated up-dip relatively slowly in the early stages of the earthquake before reaching the trench. The global-moment release rate reached its maximum at ~60 s and maintained high values until 75 s, when rupture shifted back to the deeper region and slip was widely distributed. A narrow zone of high slip emerged at the bottom of the rupture plane at ~90 s, and the major rupture finished at ~100 s. After 100 s, rupture propagated along-strike to the south with a somewhat smaller slip rate.

The highest cumulative slip in our model is ~30 m and is strongly concentrated in the shallowest part of the fault, near the trench. The values of slip rate and slip are relative in that they depend on the assumed moment of the M_w 7.3 foreshock. Aftershock hypocenters determined by the Japan Meteorological Agency are distributed around, but not inside, the large slip area. This is a common observation for earthquakes for which resolution of the slip distribution and location accuracy of the aftershocks allows a meaningful comparison (*9*, *10*). The eGf method depends on the selection of the eGf event; however, the above features are robust with respect to the assumed eGf (see SOM text and fig. S3).

Amplified motion of the hanging wall near Earth's surface is a feature expected for rupture propagation on a thrust fault with dynamic overshoot (shear stress reduction below dynamic

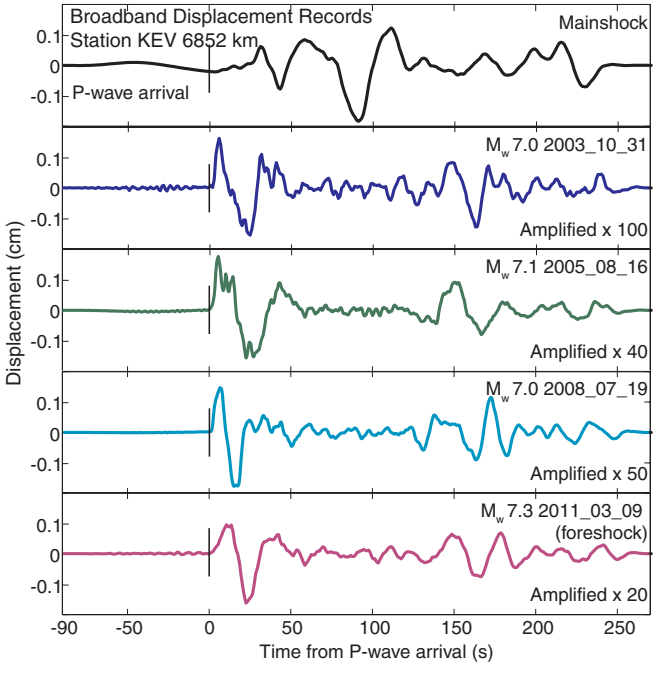

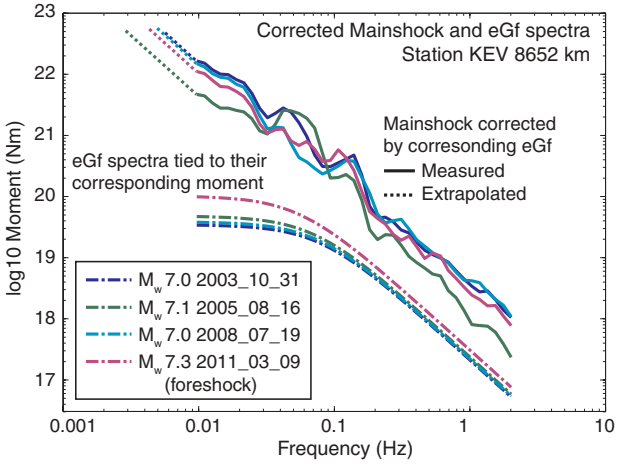

Fig. 3. (**Left**) Mainshock and eGf broadband seismograms at GSN station KEV. (**Right**) Spectra of *P*-wave train for mainshock seismograms after deconvolving different eGf events. The close correspondence of the corrected spectra indicates that our results are robust with respect to the assumed eGf; however, the moment spectra of the mainshock appears to be missing the lowest-frequency components. We extrapolated the spectra to low frequencies, as shown by the dashed lines. This is a source of uncertainty, but the amount of energy involved in the extrapolation is 18% on average, for all stations and eGf corrections.

friction), as demonstrated by numerical simulations with a free surface (*11*–*13*). The reversal of rupture propagation direction, from upward to downward, shown in Fig. 1 is a feature observed in numerical models with dynamic overshoot. In subduction zones, a relatively compliant hanging wall should amplify this effect and was recognized as playing a potentially important role in tsunamigenesis (*13*). Thermal pressurization is a possible mechanism for dynamic fault weakening as well (*14*); however, models of the effects of thermal pressurization over a broad range of the relevant fault zone properties indicate that it should be operative at very small values of slip, before substantial seismic waves are radiated (*15*). Thus, if thermal pressurization is important for part of the fault, it should be important for the entire fault.

The degree to which slip is amplified at the free surface and shear stress is reduced to below dynamic friction is underscored by several events as large as M_w 6.5 (12 March 2011) with opposite (normal) mechanisms close to the maximum slip area and landward from the trench. The waveforms of one of these events with a low-angle normal mechanism are nearly opposite from those of the M_w 7.3 foreshock, once the difference of source time functions is accounted for (fig. S4). We confirm that the normal faulting event of the M_w 6.5 aftershock is at approximately the depth of the plate interface through the comparison of surface-reflected phases with a reverse faulting foreshock (fig. S5). Although this suggests that both of these earthquakes occurred on the plate interface, even if they did not, events with opposite mechanisms would not be expected to occur without a reversal of the stress state. Complete stress drop and dynamic overshoot beyond zero shear stress has been inferred previously from aftershock-mechanism diversity or reversed aftershock mechanisms (*16*–*18*), but not in subduction zones, and never before at such a scale as implied by reversed aftershocks of the Tohoku-Oki earthquake.

Although the greatest slip is located near the trench, high-frequency waves are radiated much more strongly near the deeper edge of rupture, where much less total slip is resolved. Two groups of waves are clearly observed in the northern KiK-net stations, but only a single pulse is dominant in the southern stations (Fig. 2). The initial 40 s of rupture explains the first group of short-period waves observed only in the northern stations; however, the expected high-frequency waves from the shallower areas of massive slip are not apparent. Instead, rupture of the deep part of the fault after ~90 s is required to explain the second group of high-frequency arrivals. A single group of high-frequency waves at southern stations can be explained by sources located near the southwestern edge of our slip model.

We estimate the radiated energy of the mainshock using eGf deconvolution to isolate source spectra (*8*). We use the M_w 7.3 foreshock and three earlier events on the Japan Trench as eGfs (Fig. 3, figs. S6 and S7, and table S1), with *P*-wave coda spectra of vertical broadband displacement records at 43 GSN stations. We find that the *P*-wave spectra are deficient in low-frequency energy, potentially due to the shallow interference effect of the moment tensor components (*19*), which may explain why we had to extrapolate the source spectrum at low frequencies to match the mainshock moment.

We find a mainshock radiated energy $E_S = 9.1 \times 10^{17}$ J, averaged over all stations and all choices of eGfs. The mainshock energy estimates from each eGf event are similar, implying that the result is robust (table S1). Although we find a strong azimuthal dependence of a factor of 3 to 4 in the radiated energy due to strong directivity in the mainshock (fig. S8), our stations are well distributed azimuthally, and our mean estimate of energy reflects the unbiased mean. Nevertheless, our estimate is about twice as large as the 5.1×10^{17} J determined by the U.S. Geological Survey (USGS) (*20*). Discrepancies may be due to differences in assumed material parameters such as wave velocity and density (*21*), as well as to our extrapolation to low frequencies, which accounts for 18% of the total estimated energy (fig. S7). The scaled energy, E_S/M_o (where M_o is the seismic moment), of the mainshock is 2.0×10^{-5}, which is consistent with previous studies that show a typical scaled energy of 3×10^{-5} for ordinary earthquakes (*22*). It is clearly much larger than the 1 to 3×10^{-6} of "tsunami earthquakes" in the seismological use of the term (*23*–*25*). That is, the tsunami for the Tohoku-Oki earthquake was not anomalously large, given the seismic energy or seismic moment.

The azimuthal dependence of seismic energy estimates (fig. S8) is consistent with the slip model (Fig. 1). The direction of rupture propagation is west-north-west for 0 to 40 s and 60 to 90 s. Therefore, we have an overall directivity pattern that is approximated by a sine curve with the maximum at ~300°. In addition to this global trend, we observe sharp peaks of energy at two azimuths: ~30° and ~200°. These are close to the strike direction of the fault, and we suggest that these peaks are generated by the sudden emergence of large slip along trench at 60 s. Even though the up-dip rupture propagation is relatively slow, strong directivity can arise due to a high apparent velocity if slip is amplified in near synchrony along strike as rupture approaches the surface along the trench.

The Tohoku-Oki earthquake has two modes of rupture: (i) shallow, relatively quiet rupture with dynamic overshoot and (ii) deep rupture that radiates high-frequency waves energetically. Observations at either high or low frequencies alone would result in a misleading representation of the earthquake. The shallow slip of 30 m is large, but geodetic and tsunami modeling indicate that the slip may be even larger. In any case, it may not be sufficient to account for the accumulated plate-boundary slip because the relative plate motion is ~83 mm/year, and there is no written report of such a large earthquake since AD 1600. The shallow part of the fault may not always fail in stick-slip. Slip on the corresponding shallow part of the subduction interface in northern Japan in the 1896 Sanriku-Oki tsunami earthquake may have been relatively slow as well, because it generated a much larger tsunami than expected from the radiated seismic waves (*26*). The 1994 Sanriku-Oki earthquake (M_w 7.6) also started far from the coast and propagated landward very slowly during the first 20 s (*27*) and radiated high-frequency waves primarily from the deeper part of the fault (*28*). Finally, we note that characteristic repeating earthquakes near the deep edge of the source region of the Tohoku-Oki earthquake have relatively high seismic energy (*29*, *30*).

Our observations suggest that the two rupture modes of the Tohoku-Oki earthquake reflect variations in the frictional nature of the subduction interface with depth and explain variable earthquake behavior in the Japan Trench. We suggest that the large, shallow slip with dynamic overshoot was activated by the preceding deep energetic rupture. Had the down-dip rupture not occurred, the Tohoku-Oki earthquake could have generated a tsunami that would have been considered anomalously large. This may explain the large tsunami of the 1896 Sanriku earthquake, but what excited the shallower slip without an energetic deep rupture is unclear. Whatever the resolution to this question, rapid imaging of near-trench slip could provide timely warning that an earthquake might generate an unusually large tsunami.

References and Notes

1. D. L. Wells, K. J. Coppersmith, *Bull. Seismol. Soc. Am.* **84**, 974 (1994).
2. P. M. Mai, G. C. Beroza, *Bull. Seismol. Soc. Am.* **90**, 604 (2000).
3. S. H. Hartzell, *Geophys. Res. Lett.* **5**, 1 (1978).
4. E. Fukuyama, K. Irikura, *Bull. Seismol. Soc. Am.* **76**, 1623 (1986).
5. J. Mori, S. Hartzell, *Bull. Seismol. Soc. Am.* **80**, 507 (1990).
6. S. Ide, *Tectonophysics* **334**, 35 (2001).
7. A. Baltay, G. Prieto, G. C. Beroza, *J. Geophys. Res.* **115**, B08314 (2010).
8. Materials and methods are available on *Science* Online.
9. C. Mendoza, S. H. Hartzell, *Bull. Seismol. Soc. Am.* **78**, 1438 (1988).
10. C. H. Scholz, *The Mechanics of Earthquakes and Faulting* (Cambridge Univ. Press, Cambridge, ed. 2, 2008).
11. D. D. Oglesby, R. J. Archuleta, S. B. Nielsen, *Science* **280**, 1055 (1998).
12. D. D. Oglesby, S. M. Day, *Bull. Seismol. Soc. Am.* **91**, 1099 (2001).
13. S. Ma, G. C. Beroza, *Bull. Seismol. Soc. Am.* **98**, 1642 (2008).
14. A. Bizzarri, M. Cocco, *J. Geophys. Res.* **111**, B05303 (2006).
15. S. V. Schmitt, P. Segall, T. Matsuzawa, *J. Geophys. Res.* 10.1029/2010JB008035
16. G. C. Beroza, M. D. Zoback, *Science* **259**, 210 (1993).
17. E. Hauksson, *Bull. Seismol. Soc. Am.* **84**, 917 (1994).
18. N. A. Ratchkovski, *Geophys. Res. Lett.* **30**, 2017 (2003).
19. H. Kanamori, J. Given, *Phys. Earth Planet. Inter.* **27**, 8 (1981).
20. J. Boatwright, G. Choy, *J. Geophys. Res.* **91**, 2095 (1986).

21. We use a density ρ = 2800 kg/m^3. Using ρ = 3000 kg/m^3, which is a common choice in other energy studies, would have reduced our radiated energy by 6.5% to E_S = 8.5 × 10^{17} J.
22. S. Ide, G. C. Beroza, *Geophys. Res. Lett.* **28**, 3349 (2001).
23. H. Kanamori, *Phys. Earth Planet. Inter.* **6**, 346 (1972).
24. H. Kanamori, M. Kikuchi, *Nature* **361**, 714 (1993).
25. A. Venkataraman, H. Kanamori, *J. Geophys. Res.* **109**, B05302 (2004).
26. Y. Tanioka, K. Sataka, *Geophys. Res. Lett.* **23**, 1549 (1996).
27. W. Nakayama, M. Takeo, *Bull. Seismol. Soc. Am.* **87**, 918 (1997).
28. T. Sato, K. Imanishi, M. Kosuga, *Geophys. Res. Lett.* **23**, 33 (1996).
29. N. Uchida *et al.*, abstract S34B-04 presented at the 2010 American Geophysical Union Fall Meeting, San Francisco, CA, 13 to 17 December 2010.
30. A. Baltay, S. Ide, G. Prieto, G. Beroza, *Geophys. Res. Lett.* **38**, L06303 (2011).
31. P. Wessel, W. H. F. Smith, *Eos Trans. AGU* **72**, 441 (1991).

Acknowledgments: This work was supported by the Ministry of Education, Culture, Sports, Science and Technology of Japan KAKENHI (grant 21107007) and the Japan Society for the Promotion of Science KAKENHI (grant 23244090). GMT software (*31*) was used to draw figures. A.B. was supported at Stanford University by the Gabilan Stanford Graduate Fellowship. GSN data are available online (www.iris.edu/hq/programs/gsn/data) through a cooperative scientific facility operated jointly by the Incorporated Research Institutions for Seismology, the USGS, and the NSF. KiK-net data are also available online (www.kik.bosai.go.jp/kik/) through National Research Institute for Earth Science and Disaster Prevention.

Supporting Online Material
www.sciencemag.org/cgi/content/full/science.1207020/DC1
Materials and Methods
SOM Text
Figs. S1 to S8
Table S1
References (*32*–*34*)

4 April 2011; accepted 12 May 2011
Published online 19 May 2011;
10.1126/science.1207020

TFEB Links Autophagy to Lysosomal Biogenesis

Carmine Settembre,[1,2,3] Chiara Di Malta,[1] Vinicia Assunta Polito,[1,2,3] Moises Garcia Arencibia,[4] Francesco Vetrini,[2] Serkan Erdin,[2,3] Serpil Uckac Erdin,[2,3] Tuong Huynh,[2,3] Diego Medina,[1] Pasqualina Colella,[1] Marco Sardiello,[2,3] David C. Rubinsztein,[4] Andrea Ballabio[1,2,3,5]*

Autophagy is a cellular catabolic process that relies on the cooperation of autophagosomes and lysosomes. During starvation, the cell expands both compartments to enhance degradation processes. We found that starvation activates a transcriptional program that controls major steps of the autophagic pathway, including autophagosome formation, autophagosome-lysosome fusion, and substrate degradation. The transcription factor EB (TFEB), a master gene for lysosomal biogenesis, coordinated this program by driving expression of autophagy and lysosomal genes. Nuclear localization and activity of TFEB were regulated by serine phosphorylation mediated by the extracellular signal–regulated kinase 2, whose activity was tuned by the levels of extracellular nutrients. Thus, a mitogen-activated protein kinase–dependent mechanism regulates autophagy by controlling the biogenesis and partnership of two distinct cellular organelles.

Macro-autophagy is an evolutionarily conserved mechanism that targets intracytoplasmic material to lysosomes, thus providing an energy supply during nutrient starvation (*1*, *2*). Autophagy activation during starvation is negatively regulated by mammalian target of rapamycin complex 1 (mTORC1), whose activity is dependent on cellular energy needs (*3*). The observation that starvation induced the transcription of several autophagy genes, whereas inhibition of mTORC1 did not, suggests the presence of alternative transcriptional mTORC1-independent regulation of autophagy (*4*, *5*) (fig. S1, A and B).

We tested whether TFEB, a transcription factor ("EB") that controls lysosomal biogenesis by positively regulating genes belonging to the Coordinated Lysosomal Expression and Regulation (CLEAR) network, also regulated autophagy (*6*, *7*). Stable TFEB overexpression in HeLa cells significantly increased the number of autophagosomes detected by immunofluorescence and immunoblotting of the LC3 protein, which specifically associates with autophagosomes (*8*) (Fig. 1, A and B). Similar data were obtained by transient overexpression of TFEB in HeLa and COS7 (monkey kidney fibroblast) cells (fig. S2, A to C) and from electron microscopy on mouse embryonic fibroblasts (MEFs) infected with a lentivirus overexpressing TFEB (fig. S3, A to D). This increase persisted in cells treated with bafilomycin and pepstatin, as well as the cysteine proteinase inhibitor E64, which are lysosomal inhibitors of autophagosome and LC3-II degradation; the sustained increase indicated that TFEB activates the formation of autophagosomes (Fig. 1A and fig. S4, A and B).

RNA interference (RNAi) of *TFEB* in HeLa cells resulted in decreased levels of LC3-II both in normal and starved conditions, in either the presence or absence of bafilomycin (Fig. 1, C and D). The decrease of LC3-II correlated with the levels of *TFEB* down-regulation achieved by the different RNAi oligomers (fig. S4, C and D). These gain- and loss-of-function data suggest that the biogeneses of autophagosomes and lysosomes are co-regulated by TFEB. We next measured the rate of delivery of autophagosomes to lysosomes using an RFP-GFP (red fluorescent protein–green fluorescent protein) tandem tagged LC3 protein, which discriminates early autophagic organelles [GFP-positive and monomeric RFP (mRFP)–positive] from acidified autophagolysosomes (GFP-negative and mRFP-positive), because of quenching of the GFP signal (but not of mRFP) inside acidic compartments. The number of autophagolysosomes was higher in TFEB overexpressing cells than in control cells, which indicated that TFEB enhanced the autophagic flux (Fig. 1E). Consistently, degradation of long-lived proteins (*9*) was enhanced by TFEB overexpression and reduced by TFEB depletion (knockdown) (fig. S5A).

To test whether TFEB regulated the expression of autophagy genes, we analyzed the mRNA levels of a group of 51 genes reported to be involved in several steps of the autophagic pathway (*1*, *10*, *11*). The enhancement of the expression levels of autophagy genes in cells overexpressing TFEB was similar to that of starved cells (Fig. 2A and table S1) [Pearson correlation coefficient (r) = 0.42; P = 0.001]. Eleven of the analyzed genes were significantly up-regulated after transient, stable, and tetracycline-dependent TFEB expression, whereas they were down-regulated after TFEB silencing in both normal and starved conditions (Fig. 2A, fig. S5B, and tables S2 and S3). The expression of *UVRAG*, *WIPI*, *MAPLC3B*, *SQSTM1*, *VPS11*, *VPS18*, and *ATG9B* was most significantly affected by TFEB overexpression (tables S2 and S3). These genes are known to play a role in different steps of autophagy (fig. S6) and appeared to be direct targets of TFEB because they carry at least one TFEB target site (*6*) in their promoters (fig. S7). In addition, we validated the binding of TFEB to the target sequence by quantitative chromatin immunoprecipitation assay (QChip) and observed that this binding is further enhanced during starvation (fig. S8, A and B).

In normal conditions, TFEB is localized to the cytoplasm (*6*). Nutrient starvation rapidly induced TFEB nuclear translocation (Fig. 2, B and C), and cytosolic TFEB from starved cells

[1]Telethon Institute of Genetics and Medicine (TIGEM), Via Pietro Castellino 111, 80131 Naples, Italy. [2]Department of Molecular and Human Genetics, Baylor College of Medicine, Houston, TX 77030, USA. [3]Jan and Dan Duncan Neurological Research Institute, Texas Children's Hospital, Houston, TX 77030, USA. [4]Cambridge Institute for Medical Research, Wellcome Trust–Medical Research Council Building, Addenbrooke's Hospital, Hills Road, Cambridge CB2 0XY, UK. [5]Medical Genetics, Department of Pediatrics, Federico II University, Via Pansini 5, 80131 Naples, Italy.

*To whom correspondence should be addressed. E-mail: ballabio@tigem.it

Shallow Dynamic Overshoot and Energetic Deep Rupture in the 2011 M_W 9.0 Tohoku-Oki Earthquake

Satoshi Ide, Annemarie Baltay and Gregory C. Beroza (May 19, 2011)

Science Translational Medicine **332** (6036), 1426-1429. [doi: 10.1126/science.1207020] originally published online May 19, 2011

Editor's Summary